The Astrophysical Journal, 792:30 (14pp), 2014 September 1 doi:10.1088/0004-637X/792/1/30

INITIAL PERFORMANCE OF THE *NEOWISE* REACTIVATION MISSION

A. Mainzer[1], J. Bauer[1,2], R. M. Cutri[2], T. Grav[3], J. Masiero[1], R. Beck[2], P. Clarkson[4], T. Conrow[2], J. Dailey[2], P. Eisenhardt[1], B. Fabinsky[1], S. Fajardo-Acosta[2], J. Fowler[2], C. Gelino[2], C. Grillmair[2], I. Heinrichsen[1], M. Kendall[4], J. Davy Kirkpatrick[2], F. Liu[1], F. Masci[2], H. McCallon[2], C. R. Nugent[1], M. Papin[2], E. Rice[1], D. Royer[1], T. Ryan[4], P. Sevilla[5], S. Sonnett[1], R. Stevenson[1], D. B. Thompson[5], S. Wheelock[2], D. Wiemer[4], M. Wittman[2], E. Wright[6], and L. Yan[2]
[1] Jet Propulsion Laboratory, California Institute of Technology, Pasadena, CA 91109 USA; amainzer@jpl.nasa.gov
[2] Infrared Processing and Analysis Center, California Institute of Technology, Pasadena, CA 91125, USA
[3] Planetary Science Institute, Tucson, AZ, USA
[4] Ball Aerospace and Technology Center, Boulder, CO, USA
[5] Space Dynamics Laboratory, Utah State University, Logan, UT, USA
[6] Department of Physics and Astronomy, UCLA, P.O. Box 91547, Los Angeles, CA 90095-1547, USA
Received 2014 March 30; accepted 2014 June 23; published 2014 August 12

ABSTRACT

NASA's *Wide-field Infrared Survey Explorer* (*WISE*) spacecraft has been brought out of hibernation and has resumed surveying the sky at 3.4 and 4.6 μm. The scientific objectives of the *NEOWISE* reactivation mission are to detect, track, and characterize near-Earth asteroids and comets. The search for minor planets resumed on 2013 December 23, and the first new near-Earth object (NEO) was discovered 6 days later. As an infrared survey, *NEOWISE* detects asteroids based on their thermal emission and is equally sensitive to high and low albedo objects; consequently, *NEOWISE*-discovered NEOs tend to be large and dark. Over the course of its three-year mission, *NEOWISE* will determine radiometrically derived diameters and albedos for ~2000 NEOs and tens of thousands of Main Belt asteroids. The 32 months of hibernation have had no significant effect on the mission's performance. Image quality, sensitivity, photometric and astrometric accuracy, completeness, and the rate of minor planet detections are all essentially unchanged from the prime mission's post-cryogenic phase.

Key words: comets: general – infrared: general – minor planets, asteroids: general – space vehicles – surveys

Online-only material: color figures, machine-readable table

1. INTRODUCTION

Understanding the numbers, orbits, and physical properties of the asteroids and comets that approach Earth is essential both for characterizing the population of objects that pose a potential impact hazard, as well as for planning an appropriate mitigation strategy should one be discovered on a threatening trajectory. Of the approximately 10,700 near-Earth objects (NEOs; asteroids and comets with perihelia less than 1.3 AU) discovered to date, only the most basic properties (orbital parameters and absolute magnitude H) are known for all but ~2000 at present. Well-determined physical measurements such as taxonomic classification, sizes, and shapes and rotational states are being determined for ~100 additional NEOs each year (e.g., the MIT-UH-IRTF Joint Campaign for NEO Spectral Reconnaissance; Xu et al. 1995; Tedesco et al. 2002; Benner et al. 2008; Durech et al. 2010; Reddy 2010, and many others). Much remains to be learned about the detailed physical properties of the NEOs, particularly since the ~10,700 known NEOs represent only a small fraction of the total population at all size ranges. Recent estimates suggest that there are 20,500 ± 3000 near-Earth asteroids (NEAs) larger than 100 m in diameter; it is estimated that only ~25% of these have been discovered to date (Mainzer et al. 2011b). For sizes smaller than 100 m, survey completeness drops precipitously.

Because impact energy is proportional to diameter cubed for a given density, relatively small errors in diameter can lead to large errors in predicted impact energy. Today, the vast majority of NEOs are discovered by visible light surveys such as the Catalina Sky Survey (Larson 2007) and PanSTARRS[7]. Their observations result in a measurement of absolute magnitude H; diameter must be inferred using an assumed albedo. NEO albedos are known to range widely, from ~1% to 50% (Stuart & Binzel 2004; Mainzer et al. 2011b). Almost always, nothing beyond absolute magnitude H is known to narrow the range of possible albedos, so the uncertainty in albedo ranges from extremely dark to very bright. In this case, the error in diameter estimated from H alone using an assumed albedo is plus or minus a factor of three to four when using the relationship

$$D = \left[\frac{1329 \cdot 10^{-0.2H}}{p_v^{1/2}} \right], \quad (1)$$

where D is the effective spherical diameter (Fowler & Chillemi 1992; Bowell et al. 1989). Therefore, the uncertainty in estimated impact energy can be a factor of roughly 20 if diameter is computed using H alone. If taxonomic type can be ascertained, it can be used to restrict the range of probable albedos, although the correlation between taxonomic type and albedo is not foolproof (e.g., Stuart & Binzel 2004; Mainzer et al. 2011e, 2012b; Thomas et al. 2011). However, only a small fraction of NEOs become bright enough to be observed spectroscopically, particularly the dark asteroids that are much more difficult to detect with the visible and near-infrared spectroscopy required for taxonomic classification due to their extreme faintness (Mainzer et al. 2011e). For most NEOs, only their absolute magnitude and orbits are known, leading to large uncertainty in diameter and impact energy.

Infrared radiometry allows physical parameters such as diameter and albedo to be determined for large numbers of minor planets. An asteroid's effective spherical diameter D can

[7] http://pan-starrs.ifa.hawaii.edu/public/

be found from its emitted flux at thermal wavelengths (e.g., Lebofsky et al. 1986; Harris 1998; Tedesco et al. 2002). Diameters derived from thermal infrared measurements are less sensitive to an object's albedo than those derived purely from reflected sunlight. If high-quality photometry at multiple infrared wavelengths centered near the peak of an asteroid's thermal emission (typically ∼10 μm for ∼300 K NEOs) is available that adequately samples its rotational phase, effective spherical diameter can be determined to within ±10% (Mainzer et al. 2011c, 2011d). This error in diameter translates to a much smaller error in impact energy than that derived using only H to estimate size. Although accurate diameters can be computed using infrared measurements alone, the combination of visible and thermal measurements allows for determination of albedo, which yields clues as to whether an object is stony or carbonaceous (e.g., Tholen & Barucci 1989; DeMeo et al. 2009; Mainzer et al. 2011e, 2012b). Albedo in turn informs the likely range of densities and hence impact energy, to the extent that it can be tied to taxonomic types and compositional information through linkages to either meteoritic parent bodies (e.g., Consolmagno & Britt 1998; Binzel & Xu 1993; Buratti et al. 2013) or direct measurements of asteroid density (e.g., Carry 2012; Merline et al. 2002).

NASA's *Wide-field Infrared Survey Explorer* (*WISE*) mission surveyed the entire sky simultaneously in four infrared wavelengths (3.4, 4.6, 12, and 22 μm; denoted *W*1, *W*2, *W*3, and *W*4 respectively) with significant improvements in spatial resolution and sensitivity compared to its predecessors (*WISE*; Wright et al. 2010; Cutri et al. 2012). The spacecraft is in a Sun-synchronous polar orbit around the Earth that allows for continuous observations near 90° solar elongation. Over the course of its one-year prime mission, the asteroid-hunting portion of the project known as *NEOWISE* detected and reported radiometrically derived diameters and albedos for >158,000 asteroids, including ∼700 NEOs (Mainzer et al. 2011a). More than 160 comets were detected; the infrared data have been used to constrain nucleus sizes, particle size distributions, and gas abundances (Bauer et al. 2013, 2012b, 2011; Stevenson et al. 2012). *NEOWISE* detections have been used to set limits on the numbers, orbital elements, sizes, and albedos of asteroid populations throughout the inner solar system (e.g., Mainzer et al. 2011b, 2012b; Mainzer et al. 2014; Masiero et al. 2011; Grav et al. 2011b, 2012a; DeMeo & Carry 2014).

The *WISE* mission surveyed the sky 1.2 times until its dual-stage solid hydrogen cryostat was depleted on 2010 September 30. The mission was extended an additional 4 months in order to complete the survey of the inner edge of the main asteroid belt. The solid hydrogen was required to cool the 12 and 22 μm channels, but the 3.4 and 4.6 μm HgCdTe detector arrays continued to operate nominally after the depletion of the cryogen. The telescope optics and focal planes equilibrated near 73.5 K through passive cooling by continuously pointing near zenith.

Over the course of the four-month post-cryogenic phase of the prime mission, ∼13,500 minor planets were detected in the *W*1 and *W*2 channels, including 88 NEOs. Diameters and albedos derived from the observations at 3.4 and 4.6 μm were compared with those computed using 3.4, 4.6, 12, and 22 μm data. Since the shorter wavelengths span only the Wien side of a typical NEO or Main Belt asteroid's blackbody curve, the effective spherical diameters derived from these measurements alone are less precise, but still accurate to within approximately ±25% (Masiero et al. 2012; Mainzer et al. 2012b).

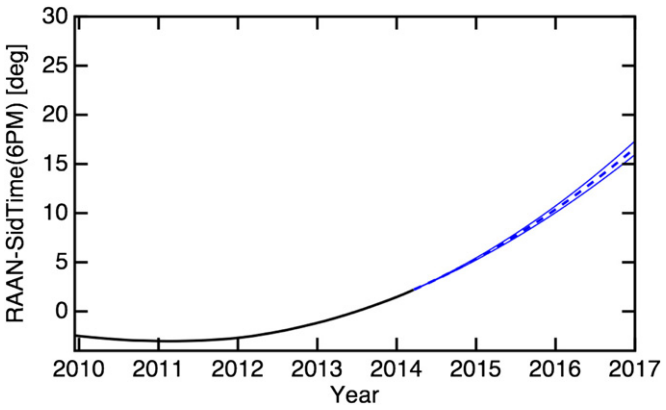

Figure 1. Change in right ascension of the ascending node (RAAN) of the *WISE* spacecraft's orbit as a function of time; measurements are shown as a solid line, and the extrapolated change based on them (bracketed by 2σ errors) is shown as a dashed line.

(A color version of this figure is available in the online journal.)

WISE survey operations were halted on 2011 February 1 after 9 months of fully cryogenic operations and 4 months of post-cryogenic operations. On 2011 February 17, the *WISE* spacecraft was then placed into a hibernation state, and communications with it ceased. In this mode, the telescope was inertially pointed near the north ecliptic pole, with the solar arrays facing the Sun. Because they viewed the warm Earth for half of each orbit, the telescope and focal planes warmed to ∼200 K.

In order to continue rapidly surveying and obtaining measurements of minor planet physical properties, the *WISE* spacecraft was brought out of hibernation on 2013 October 3. Although the solid hydrogen is now depleted, it is possible to radiatively cool the telescope to low enough temperatures that its heat does not significantly affect sensitivity. Now known as *NEOWISE*, the mission is expected to continue until 2017.

2. *NEOWISE* REACTIVATION MISSION

The scientific objectives of the *NEOWISE* reactivation mission are to discover and characterize NEOs using its 3.4 and 4.6 μm channels. The mission lifetime is limited to ∼3 yr because the spacecraft's orbital plane is slowly drifting from its ideal Sun-normal orientation under the influence of atmospheric drag (Figure 1). The *WISE* spacecraft carries no onboard propulsion system, so the rate at which the orbit changes depends solely on the degree to which solar activity affects atmospheric drag forces. After early 2017, it is anticipated that it will become increasingly difficult to keep light from the Earth and scattered sunlight out of the telescope baffle, bringing a natural end to the mission.

In order to radiatively recool the telescope and detectors, the spacecraft was once again pointed near zenith beginning in 2013 October. After approximately 3 months, the telescope temperature reached 74 K, completing the cool-down process (Figure 2). During this time, the spacecraft's subsystems were checked out, and high-rate communications via Ku-band link to NASA's Tracking and Data Relay Satellite System and the accompanying ground system in White Sands, New Mexico were reestablished. The first images from the *WISE* spacecraft after reactivation were obtained on 2013 December 7 at a telescope temperature of 76.5 K (Figures 3 and 4). The flight system began survey operations on 2013 December 13; from December 13 until December 23, a procedure to verify synchronization

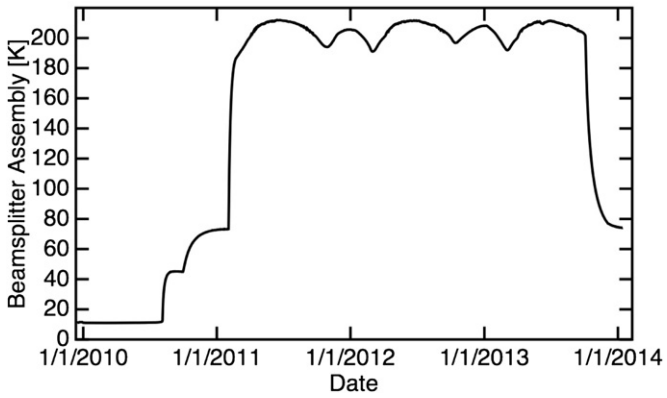

Figure 2. Temperature of the beamsplitter assembly that holds both *W*1 and *W*2 detectors as a function of time. In the hibernation state, the *WISE* spacecraft was pointed at the north ecliptic pole; consequently, temperatures throughout the payload, including the telescope structure and focal planes, rose to ∼200 K. Following the start of the *NEOWISE* survey, the telescope was repointed near zenith, causing the telescope and focal planes to cool via radiation.

between the scan mirror and spacecraft scan rate was executed, and science data processing pipeline calibrations were improved. Regular survey operations, including the moving object processing pipeline, began on 2013 December 23; the first new NEO was discovered 6 days later.

The *NEOWISE* operational cadence remains identical to that employed during the prime mission (Wright et al. 2010; Heinrichsen & Wright 2006). The telescope scans continuously along great circles with approximately constant ecliptic longitude, while a scan mirror freezes the sky on the focal planes for 9.9 s and returns to its starting position 1.1 s later. While the sky is fixed on the focal planes, simultaneous exposures are collected in the *W*1 and *W*2 bands through the use of beamsplitters every 11 s with an exposure time of 7.7 s. The 47 × 47 arcmin field of view scans at 92.°5 solar elongation, with 10% overlaps in the in-scan direction. The scan path progresses 1° day^{-1} as the Earth orbits the Sun. From 2013 December 23 to 2014 March 30, coverage at least one frame deep over 60% of the entire sky has been achieved (Figure 5). On average, 12 independent exposures are collected for each point on the ecliptic. Because the ecliptic poles are densely covered, data downlinks and momentum unloading via magnetic torque rods are always executed near the poles where data loss has minimal impact on science objectives.

As during the prime mission, science data ingest, processing, and archiving is performed at the California Institute of Technology's Infrared Processing and Analysis Center (IPAC) using the data system described in the *WISE* Explanatory Supplement for the post-cryogenic phase of the mission (Cutri et al.

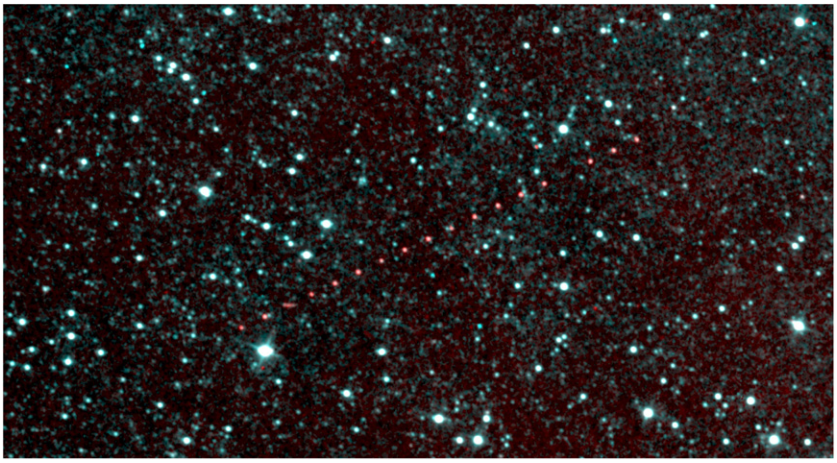

Figure 3. Coadded image using some of the first frames collected by the reactivated *NEOWISE* mission. Band *W*1 has been color-coded blue, and *W*2 is color-coded red. This coadd was made without outlier rejection to preserve the moving objects. Main Belt asteroid (872) Holda appears as a string of red dots.
(A color version of this figure is available in the online journal.)

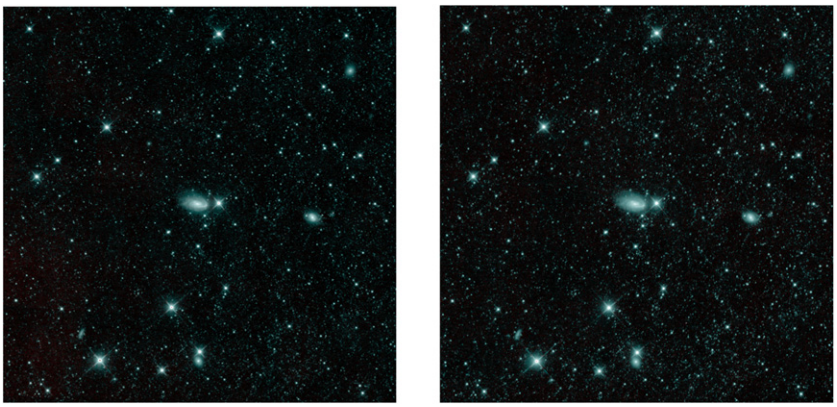

Figure 4. 60 × 60 arcmin images created from two different phases of the mission of the same patch of sky. Left: coadded exposures from the prime mission's post-cryogenic phase. Right: coadd created from exposures obtained from the reactivated *NEOWISE* mission.
(A color version of this figure is available in the online journal.)

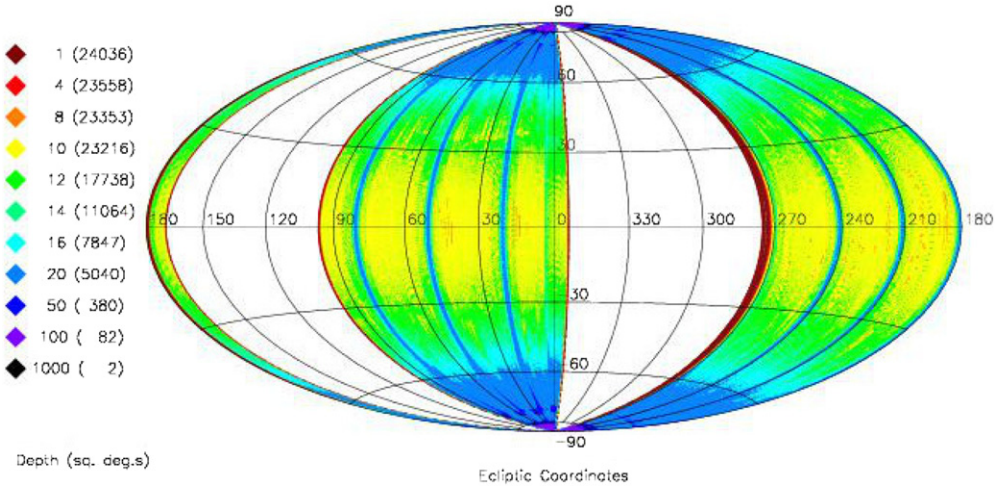

Figure 5. Depth of coverage map achieved by the *NEOWISE* mission over the first 3 months of survey operations. The numbers on the left denote the sky area with that depth of coverage or greater, along with the corresponding number of square degrees.

(A color version of this figure is available in the online journal.)

2012).[8] *NEOWISE* engineering telemetry and science image data are received and merged at IPAC twice per day following downlink from the spacecraft. The scan/frame pipeline performs basic image calibration, detects and characterizes sources on the individual images, applies astrometric and photometric calibrations, and flags sources that are positionally associated with the expected position of image artifacts. Identification of moving object candidates does not require the images to be coadded together; hence, only single exposure processing is performed. The *NEOWISE* single exposure images and extracted source databases will be publicly released via the IPAC/NASA Infrared Science Archive on an annual basis, starting in 2015 March.

3. SCIENCE OBJECTIVES AND PRELIMINARY PERFORMANCE

Based on its present rate of NEO observations, over the course of its three year mission, *NEOWISE* is expected to observe ∼2000 NEOs, roughly 700–800 of which will be detected in single-exposure images, with the remainder being recoverable through stacking. Since the observing cadence results in an average of ∼12 detections spaced evenly over ∼1.5 days, it is possible to recover many objects just below the single-exposure detection threshold by creating comoving stacks of images of previously known objects (cf. the methods described in Masci & Fowler 2009; Masci 2013; Mainzer et al. 2014). As with the prime mission, *NEOWISE* is particularly effective at discovering dark NEOs that are preferentially missed by visible light surveys. Radiometrically derived diameters and albedos for all minor planets detected during the survey will be delivered to NASA's Planetary Data System.

By virtue of the fact that the spacecraft always observes close to 90° solar elongation, 25% of the NEOs detected by *NEOWISE* are classified as PHAs. Although ground-based surveys dominate discoveries of PHAs, they constitute a decreasing fraction of their NEO discoveries; in 2013, 8% of NEOs discovered by ground-based surveys were PHAs. The NEOs and PHAs observed by *NEOWISE* during the post-cryogenic phase of the prime mission tended to be large, with a median diameter of ∼800 m. Unlike visible light surveys, which have difficulty detecting low albedo objects, the *NEOWISE* discoveries tended to be darker than the populations discovered by other surveys (Mainzer et al. 2011b).

During the prime mission's post-cryogenic phase, the first known Earth Trojan, 2010 TK_7, was discovered (Connors et al. 2011), along with another long-lived Earth co-orbital, 2010 SO_{16} (Christou & Asher 2011). As an Earth Trojan librating around the L4 Lagrange point, 2010 TK_7 spends most of its time in the daylight sky and was discovered because *WISE* observes continuously near the twilight–dawn skies where ground-based surveys can spend only a little time. The asteroid's libration only carries it as far as ∼95° solar elongation. The question as to whether or not 2010 TK_7 represents the first of a larger population of Earth Trojans remains an open one, along with how long ago such a population might have been trapped into resonance with the Earth (Tabachnik & Evans 2000). By continually surveying near 92°.5 solar elongation for three years, the mission will set significantly stricter limits on the population of Earth co-orbitals such as 2010 TK_7 and 2010 SO_{16}.

Over the course of the three-year *NEOWISE* mission, the entire sky will be observed six times at 3.4 and 4.6 μm. Tens of thousands of Main Belt asteroids and Jovian Trojans will be detected. The data will also enable a wide range of studies for transient phenomena such as high proper motion, nearby cool stars, variable stars and active galaxies, galactic novae, and supernovae.

3.1. Preliminary System Performance

Instrument performance remains nearly identical to that observed during the prime mission's post-cryogenic phase. The number of pixels with high dark current has increased slightly, most likely due to radiation effects. HgCdTe arrays' dark current levels vary strongly with temperature (Beletic et al. 2008); since *NEOWISE* is passively cooled, dark current could change slightly if temperature varies with seasons. Since the reactivation, 3.3% and 4.3% of pixels in bands *W*1 and *W*2 have been masked off due to high dark current, compared with 1.9% and 2.5% for *W*1 and *W*2 during the prime mission's post-cryogenic phase.

Figure 6 shows a comparison of the *W*1 and *W*2 profile fit photometry from a set of two *NEOWISE* single exposures

[8] http://wise2.ipac.caltech.edu/docs/release/allsky/expsup/sec8_1.html

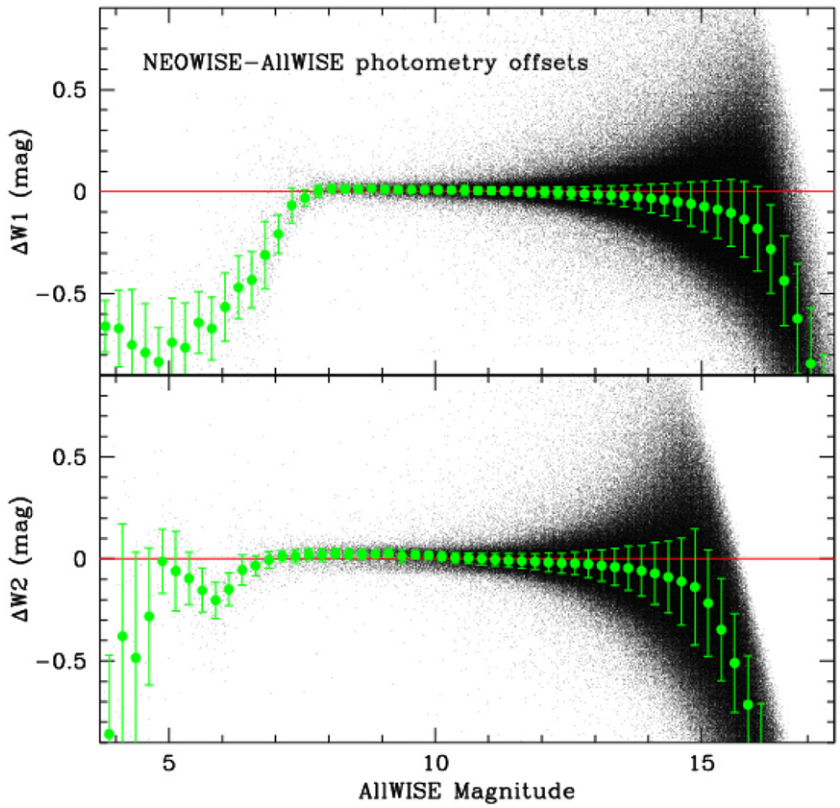

Figure 6. Difference between *W*1 (top) and *W*2 (bottom) profile-fit magnitudes measured in all single-exposures in one reactivated *NEOWISE* scan and those from the AllWISE Source Catalog, plotted as a function of AllWISE Catalog magnitude. Black dots are individual sources. Green filled circles and error bars are the trimmed average and rms of the differences for all sources in 0.25 mag wide bins.

(A color version of this figure is available in the online journal.)

compared with the same objects in the much deeper AllWISE Catalog (Cutri 2014; Cutri et al. 2013). There are essentially no shifts in zero points for either band or flux-dependent biases over most of the brightness range. The dramatic flux overestimation of *NEOWISE* fluxes brighter than the saturation levels are consistent with what was observed during the prime mission's post-cryogenic phase.

The systematic overestimation of *NEOWISE* fluxes relative to the deeper AllWISE Catalog at the faint end of the distributions is the well-known Eddington bias (Eddington 1913) that affects measurements of objects near the signal-to-noise detection threshold of any survey. Faint objects will be preferentially detected when measurement noise drives their apparent brightness above the signal-to-noise threshold. The same objects will not be detected if negative noise excursions drive their brightness down below the threshold. This statistical effect can be thought of as an asymmetric truncation of the natural distribution of measured values in the presence of random noise. Measurements of the truncated distribution will be biased toward positive values, and the amplitude of this bias increases with decreasing signal-to-noise, as shown in Figure 6. This effect was described in the Explanatory Supplement for the *Infrared Astronomical Satellite* (Beichman et al. 1988). If the Eddington bias is not accounted for, fluxes of faint sources will be overestimated. For example, in a survey in two bands with different detection limits, failure to account for the Eddington bias could result in an erroneous prediction of color changes as a function of asteroid size. For asteroids detected at thermal infrared wavelengths, the effect is most problematic for faint objects with only a small number of detections and usually results in an overestimate of size. However, most *NEOWISE*-detected minor planets have ∼10–12 observations spaced evenly over ∼36 hr. An estimate of the systematic effects of the bias in asteroid size estimates made from sparse measurements can be found in Mainzer et al. (2014).

The very slight systematic increase in $\Delta W2$ in Figure 6 over the range $7 < W2 < 14$ mag is also consistent with what was observed during the prime mission's post-cryogenic phase. The deviation is 0.03–0.04 mag, with a mean near zero. Systematic changes in *W*1 are <0.01 mag. Figure 7 compares the measured right ascension and declination between *NEOWISE* and AllWISE sources as a function AllWISE Catalog *W*1 magnitude; no offsets are observed.

We have compared the sensitivity of exposures obtained from the *NEOWISE* reactivation with those collected during the prime mission's post-cryogenic phase. The *WISE* Multiframe pipeline (Cutri et al. 2012) was run on a region of sky (Atlas Tile 0368m197) that was fully covered during both the prime mission post-cryogenic phase and the reactivated *NEOWISE* survey. The analysis was restricted to sources having >10 exposure coverages. The Multiframe pipeline produces a coadd of all exposures, as well as lists of extracted sources and their associated photometry from the coadd. Additionally, the Multiframe pipeline also measures the rms of the fluxes of each source measured on the individual frames, as well as the single-exposure detection statistics. These give some measure of the photometric measurement accuracy and single-exposure completeness. Figure 8 shows that the current *NEOWISE* average photometric repeatability is essentially identical to the prime mission's post-cryogenic phase. Figure 9 shows how the source detection completeness on the single-exposure images varies with source

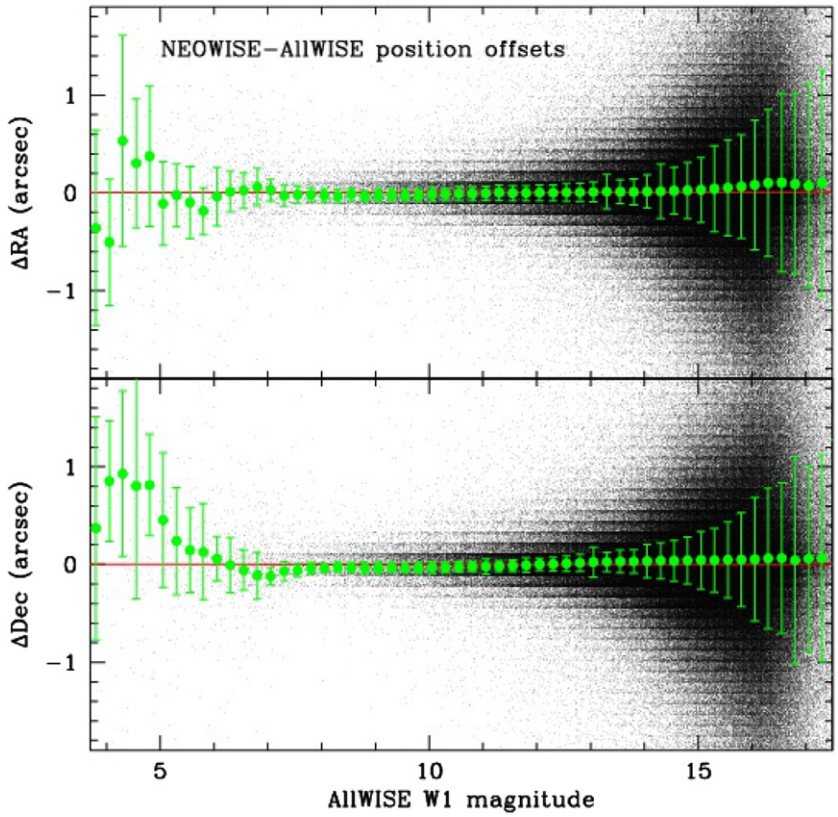

Figure 7. Differences between reconstructed right ascension (top) and declination (bottom) positions for sources in one reactivated *NEOWISE* scan. Color coding is the same as in Figure 6.

(A color version of this figure is available in the online journal.)

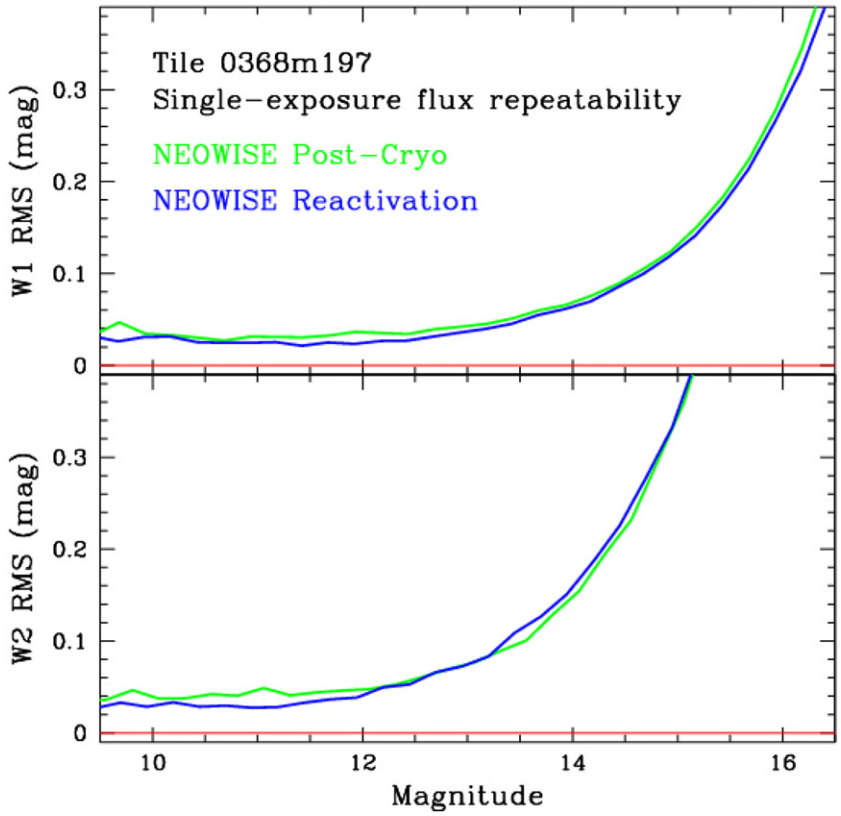

Figure 8. rms of multiple single-exposure flux measurements, in magnitude units, plotted as a function of *W*1 (top) and *W*2 (bottom) source magnitude. Reactivated *NEOWISE* measurements are shown in blue, and original post-cryogenic phase measurements are shown in green.

(A color version of this figure is available in the online journal.)

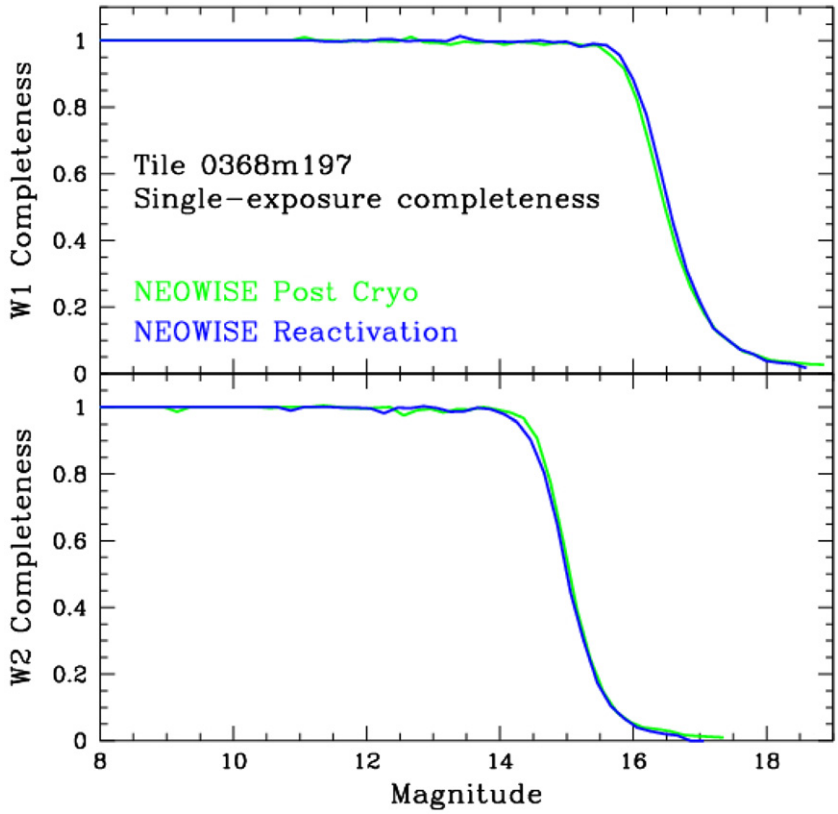

Figure 9. Single-exposure detection completeness as a function of *W*1 (top) and *W*2 (bottom) for the same objects measured in the reactivated *NEOWISE* mission (shown in blue), and the original post-cryogenic phase (green).

(A color version of this figure is available in the online journal.)

brightness. The completeness is estimated using the repeated observations of the same region of sky obtained using the *NEOWISE* survey strategy. The completeness for sources within each 0.2 mag wide brightness bin is computed by forming the ratio of the total number of times all sources within the bin are detected with signal-to-noise ratio (S/N) > 2 to the total number of times they are observed.

3.2. Moving Object Detection

Moving object candidates are identified in the *NEOWISE* data in a fashion similar to that performed during the prime mission with a number of improvements incorporated as a result of continued data analysis since the end of survey operations in 2011 (Mainzer et al. 2011a). The system is collectively known as the *WISE* Moving Object Processing System (WMOPS). Source lists for a given single exposure are assembled and compared to source lists in overlapping single exposures; sources that are co-located on separate frames within a radius of 5 arcsec are considered stationary and are eliminated from further consideration. Detections of sources that remain after stationary object rejection are removed from consideration if they fall below a flux S/N of 4.5. Pairs of detections are linked together into "tuples," then pairs are linked using the methods of Kubica et al. (2007). The Kubica et al. (2007) method uses hierarchical data structures called k-d trees to recursively partition the sources that could potentially be linked into smaller subsets, with the net result being that the search time is proportional to $\rho log\rho$ (where ρ is the source sky-plane density) instead of ρ^2. Links can only be made when detections obey velocity limits of 5° day^{-1}, and adjacent detections (separated by only 11 s) that fall into the overlap regions between single exposures are not used in the construction of the initial tuple pairs of detections. The resulting sets of position-time pairs are known as "tracklets." A minimum of five detections are required to construct a tracklet in order to ensure that the object is real and not merely a chain of cosmic rays or other noise sources.

Tracklets for which all detections cannot be associated with a previously known solar system object are visually examined by quality assurance astronomers. An example of an automatically generated quality assurance page is shown in Mainzer et al. (2011a). Tracklets are required to be reported to the International Astronomical Union's (IAU) Minor Planet Center (MPC) within 10 days of the midpoint of their observation on board the spacecraft. This requirement ensures that the uncertainty in NEO candidates' ephemerides does not grow beyond ∼1°; uncertainties much larger than this exceed the fields of view of most available follow-up facilities. With an average observational arc of ∼1.5 days, but as little as ∼0.4 day, ground-based follow-up is essential to secure NEO candidates' orbits. As during the prime mission, *NEOWISE* observations alone are generally of insufficient length to declare NEO candidates officially discovered. At present, WMOPS is run three times per week. The average achieved lag time between tracklet endpoint and delivery to the MPC is approximately 2.4 days (Figure 10).

As during the prime mission, follow-up observations of *NEOWISE* NEO candidates are essential for securing orbits. Furthermore, visible light observations are necessary for the determination of albedo (e.g., Lebofsky & Spencer 1989; Harris

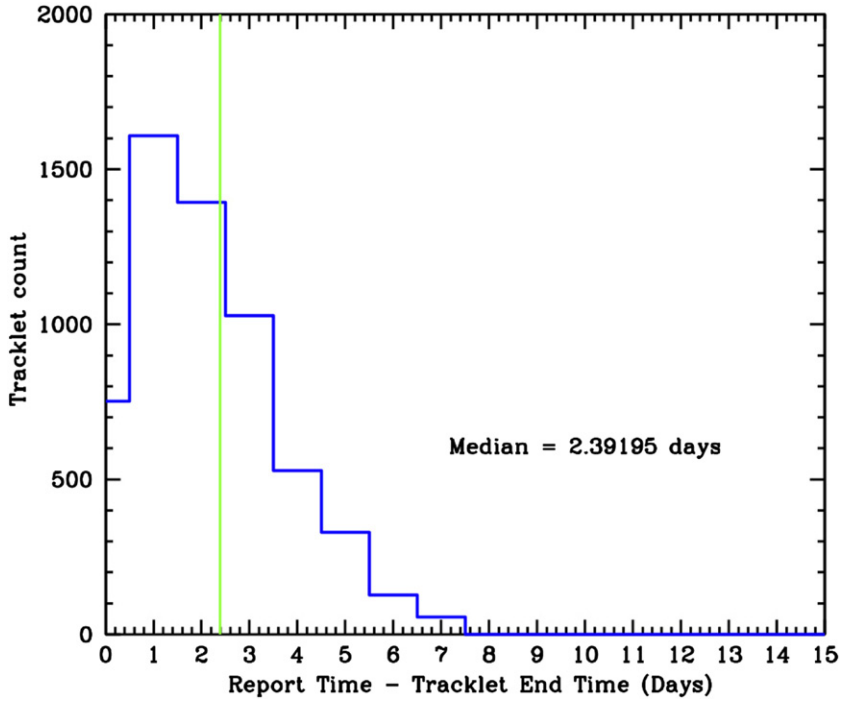

Figure 10. Distribution of delivery dates for tracklets from the reactivated *NEOWISE* mission to the Minor Planet Center, including both previously known minor planets and potential new discoveries. The mission is required to deliver tracklets within 10 days of observation.

(A color version of this figure is available in the online journal.)

1998). Candidates are placed onto the MPC's public NEO Confirmation Page.[9] Ground-based follow-up is carried out by a network of amateur and professional astronomers around the globe. Because *NEOWISE* discoveries are more likely to be dark (Figure 15), visible magnitudes can be extremely faint; most of the objects were recovered with $V \sim 21$–23 mag. Given the all-sky observing strategy, targets are often found at high or low declinations, regardless of lunar phase or weather, resulting in unique challenges for follow-up observers. Follow-up observations are critical to achieving the mission's scientific objectives, and the project greatly appreciates the contributions made by the NEO observing community. To date, only one *NEOWISE* NEO candidate out of 10 has been lost due to lack of follow-up.

4. PRELIMINARY RESULTS

The *NEOWISE* mission's minor planet detection efficiency is very similar to that achieved during the post-cryogenic phase of the prime mission. In the 90 days following the survey start on 2013 December 23, WMOPS has recorded detections of 2915 minor planets, of which 62 are NEOs and 10 are comets (Figure 11, left). This number includes 10 new NEOs discovered by *NEOWISE*, along with one new comet, C/2014 C3 *NEOWISE*, a Halley family retrograde comet discovered on 2014 February 14. The first new NEO, 2013 YP_{139}, was discovered 6 days after the start of survey operations (Figure 12). All but two of the NEOs discovered by *NEOWISE* to date have been extremely dark, with albedos lower than ~0.05. The number of NEO detections, $\sim 0.68 \pm 0.09$ day^{-1}, is similar to the rate achieved during the post-cryogenic phase of the prime mission (88 unique NEOs detected in 4 months, or 0.73 $\pm$ 0.11 day^{-1}). The NEO detection rate has been lowered due to the effects of confusion in the galactic plane in 2014 March (Figure 11, right); NEO detection rates will increase once the scan circle moves past the galactic plane. Of the thousands of Main Belt asteroids that have been observed to date, ~75% were also detected during the prime mission; *NEOWISE* re-detections from different viewing geometries offer the opportunity to perform more detailed lightcurve analyses in order to constrain shapes, rotational states, and thermophysical properties.

It is possible to evaluate the astrometric precision of the *NEOWISE* observations of minor planets in an independent way by comparing the residual fits to objects with extremely well-known orbits, e.g., numbered objects. Figure 13 shows the astrometric residual errors in right ascension and declination; the root sum square of the medians of these, ~0.67 arcsec, is identical to that observed during all phases of the prime mission.

Using the Near-Earth Asteroid Thermal Model (NEATM; Harris 1998) and the methodology described for fitting data from bands *W*1 and *W*2 only in Mainzer et al. (2012a) and Masiero et al. (2012), diameters and albedos computed for objects observed during both the fully cryogenic portion of the prime mission and the *NEOWISE* reactivation mission can be compared. The thermal model implementation includes both thermal emission and reflected sunlight; thermal modeling can only be performed if at least one of the bands is thermally dominated. It was shown in Mainzer et al. (2011c) and Mainzer et al. (2011d) that diameters derived from thermal fits performed using *WISE* 12 and 22 μm observations produced results accurate to within $\pm$10% and $\pm$25%, respectively, when compared to effective spherical diameters and albedos determined from alternate methods such as radar imaging or spacecraft visits. A comparison of thermal fits for ~1200 Main Belt asteroids detected during both the fully cryogenic prime *WISE* mission at 12

[9] http://minorplanetcenter.net/iau/NEO/toconfirm_tabular.html

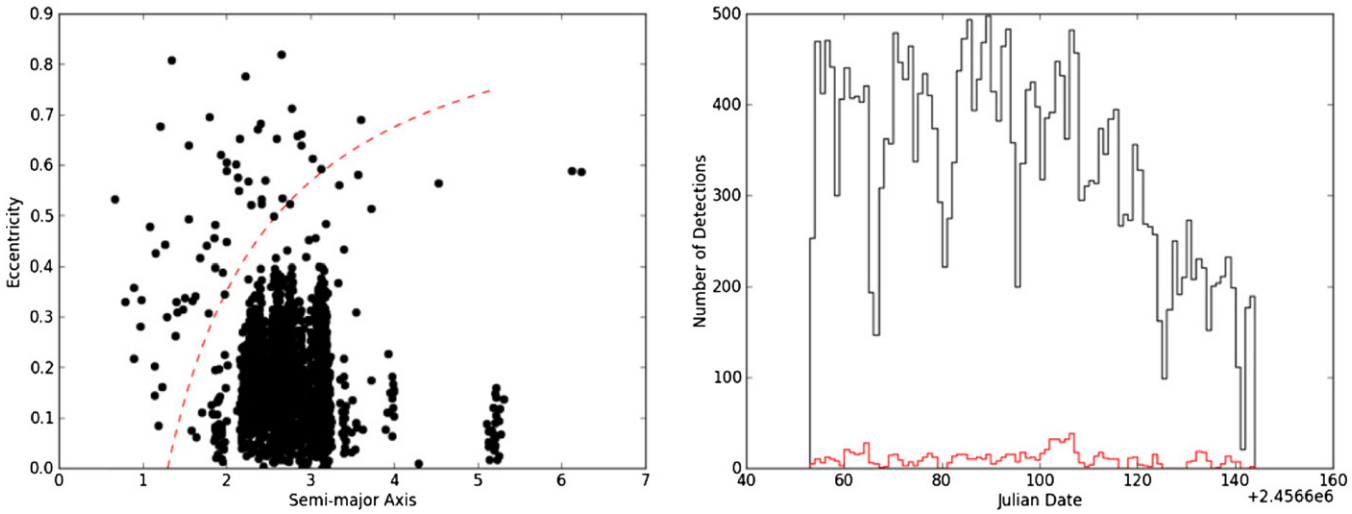

Figure 11. Left: detections as a function of time for all minor planets observed by *NEOWISE* (black line) and NEOs (red line). Minor planet detections decrease during the period when the scan circle crosses through the Galactic Center. Right: the semi-major axis vs. eccentricity of minor planets detected by the reactivated *NEOWISE* mission from the first month of survey operations; objects to the left of the red dashed line are NEOs.

(A color version of this figure is available in the online journal.)

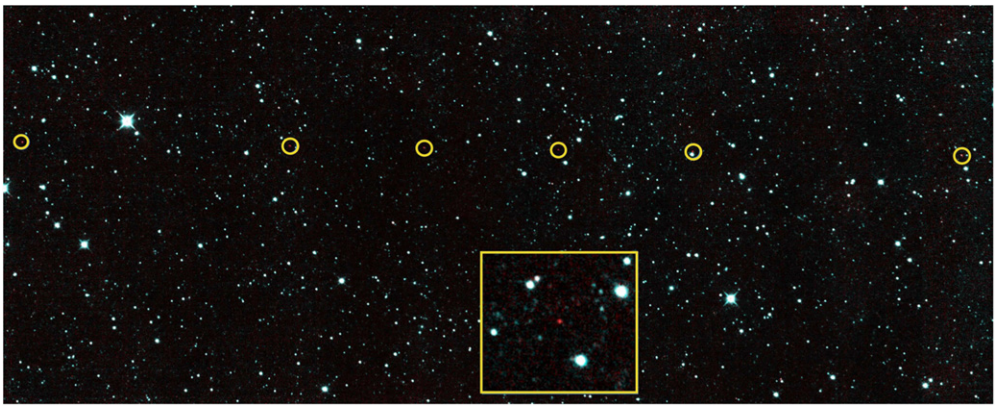

Figure 12. First new NEO discovered by the reactivated *NEOWISE* mission, 2013 YP_{139} (circled), is revealed to be large, 660 ± 190 m, and dark. The inset shows a zoomed-in view of one of the detections. This image covers ∼1.°5 of sky; the six detections span 0.4 day.

(A color version of this figure is available in the online journal.)

and/or 22 μm and during the *NEOWISE* mission at 3.4 and/or 4.6 μm has been made in order to assess the accuracy of diameters and albedos (Figure 14). For these fits, the ratio of the 3.4 μm albedo to the visible albedo (p_{IR}/p_V) and the beaming parameter η must be assumed; these are taken to be 1.4 ± 0.5 and 1.0 ± 0.2 per Masiero et al. (2012). Uncertainties in H are taken to be ±0.3 mag. The IAU phase slope parameter G is assumed to be 0.15 ± 0.10 unless independent measurements were available for a given object from Warner et al. (2009) or Pravec et al. (2012); otherwise, H values were taken from the MPC. As with Mainzer et al. (2011d), errors are determined through Monte Carlo trials that vary $W1$, $W2$, H, and G within their respective error bars.

Figure 14 shows that diameters agree to within ±21%, and albedos to within approximately ±35% of their value (e.g., an object with a 5% albedo has an uncertainty of ±2%). These results are very similar to the post-cryogenic phase of the prime mission, which showed that diameters could be determined to within ±25% and albedos to within ±40% (Mainzer et al. 2012a; Masiero et al. 2012). As was observed in these papers, the NEATM tends to underestimate the albedos of dark objects and overestimate the albedos of bright objects. A possible explanation is dark, carbonaceous asteroids tend to have gray or neutral colors, leading to a lower infrared albedo; Mainzer et al. (2011e, 2012b) found that the mean value of p_{IR}/p_V is closer to ∼1.0 for C-types. Similarly, asteroids with red-sloped visible and near-infrared spectra tend to have higher infrared albedos. Refitting dark asteroids with p_{IR}/p_V closer to 1.0 increases the resulting albedos slightly.

It is worth noting that if at least one of the two bands is not thermally dominated, then the data cannot be used for thermal modeling. All of the NEO thermal fits shown in Tables 1 and 2 are thermally dominated in $W2$. Masiero et al. (2012) describes the falloff in reflected light versus heliocentric distance and p_{IR} in band $W2$ for the Main Belt asteroids observed during the post-cryogenic phase of the prime mission. For dark asteroids, the $W2$ signal becomes thermally dominated by ∼4 AU.

Preliminary thermal fit results for the first 59 NEOs detected by *NEOWISE* are shown in Figure 15. As was observed during the prime mission, *NEOWISE* NEO discoveries are usually large (with an average diameter of ∼800 m) and low albedo, filling an area of discovery phase space that is harder for ground-based visible light surveys to cover. These properties of the *NEOWISE* survey are a result of the wavelength and observing strategy.

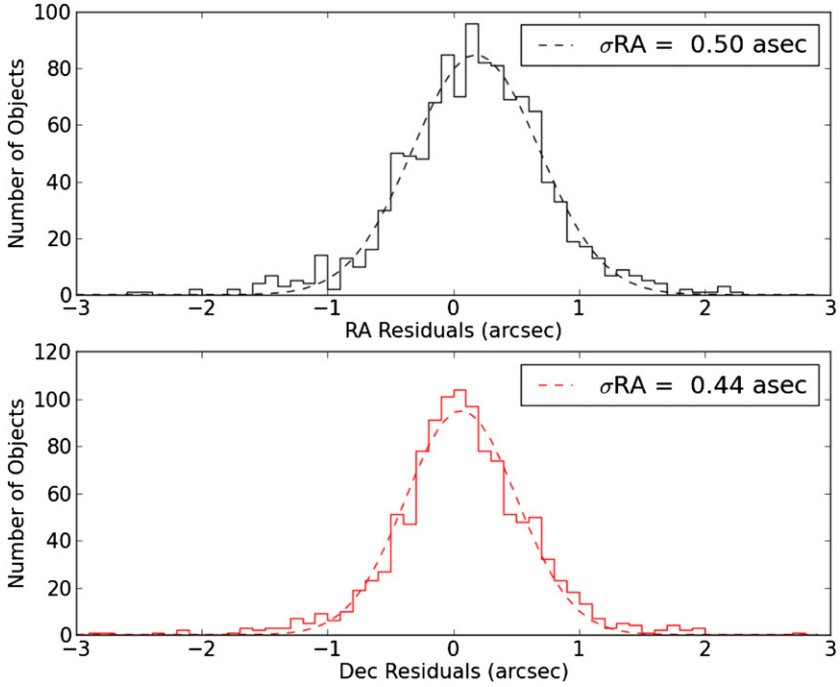

Figure 13. Residual astrometric errors resulting from fits of individual *NEOWISE* observations to numbered minor planets.
(A color version of this figure is available in the online journal.)

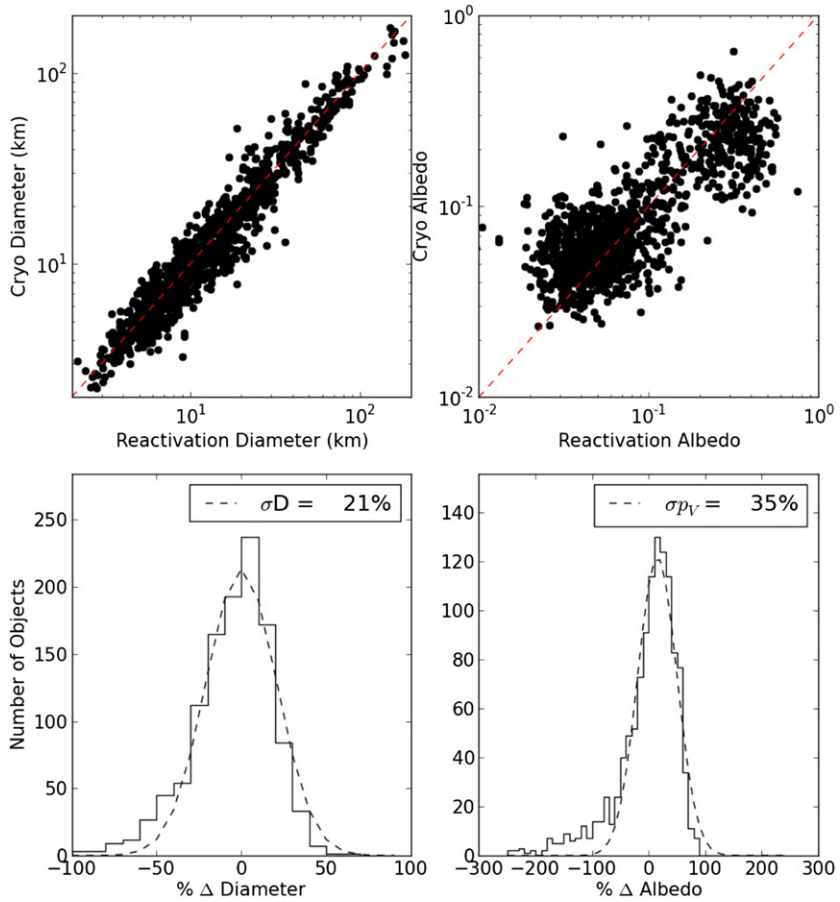

Figure 14. Upper left, right: comparison of effective spherical diameters and albedos for asteroids observed at both 12 and/or 22 μm during the prime mission and at 3.4 and/or 4.6 μm during the *NEOWISE* survey to date. A one-to-one relationship is shown in both plots as a dashed red line. Lower left, right: histogram of differences between 12 μm and 4.6 μm *NEOWISE* reactivation fits for diameter and albedo; Gaussian fits are shown as dashed black lines.
(A color version of this figure is available in the online journal.)

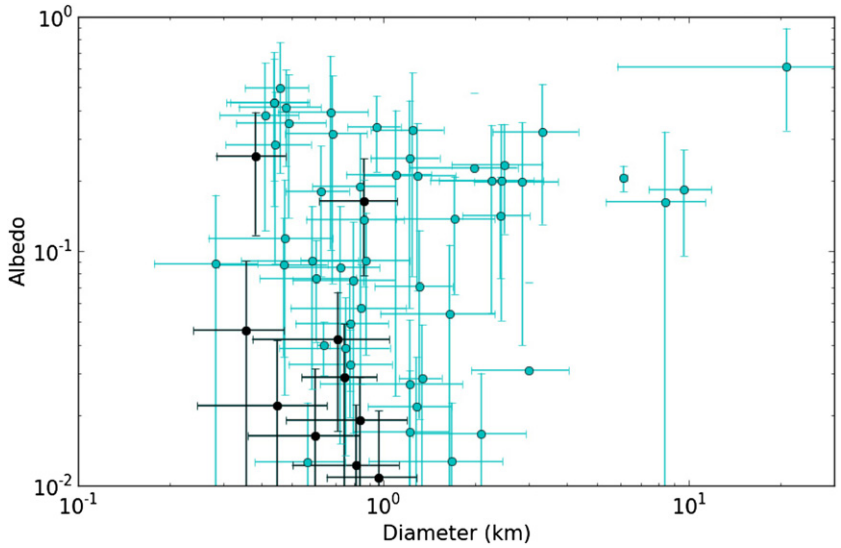

Figure 15. Preliminary diameters vs. albedos for the NEOs detected by the reactivated *NEOWISE* mission to date; *NEOWISE* discoveries are shown as black points. (A color version of this figure is available in the online journal.)

Table 1
Preliminary *NEOWISE* Magnitudes for the NEOs Shown in Figure 15 at each Observation's Modified Julian date (MJD)

Name	MJD	*W*1 (mag)	*W*2 (mag)	Aperture
01627	56676.9179688	14.682 ± 0.080	13.280 ± 0.083	0
01627	56677.1835938	14.236 ± 0.058	13.240 ± 0.079	0
01627	56677.3125	14.203 ± 0.114	13.190 ± 0.084	0
01627	56677.3125	14.382 ± 0.076	13.059 ± 0.074	0
01627	56677.3789062	14.316 ± 0.060	13.370 ± 0.100	0
01627	56677.5117188	14.379 ± 0.065	13.178 ± 0.079	0
01627	56677.578125	14.429 ± 0.069	13.249 ± 0.083	0
01627	56677.6445312	15.603 ± 0.170	14.390 ± 0.213	0
01627	56677.7070312	14.210 ± 0.055	12.997 ± 0.073	0
01627	56677.7734375	14.254 ± 0.059	13.376 ± 0.087	0

Notes. Objects that were not detected at a particular wavelength represent 2σ upper limits (Cutri et al. 2012). A value of "–" indicates that no data were available at that wavelength. The final column gives the aperture radius in arcsec used for aperture photometry; "0" indicates that the pipeline profile fit photometry was used.

(This table is available in its entirety in a machine-readable form in the online journal. A portion is shown here for guidance regarding its form and content.)

The preliminary *NEOWISE* photometry and thermal fit results for these objects are given in Tables 1 and 2.

Default values of $\eta = 1.4 \pm 0.5$ and $p_{IR}/p_V = 1.6 \pm 1.0$ were used following Mainzer et al. (2012a), unless both *W*1 and *W*2 were thermally dominated (allowing η to be fit) or unless η and p_{IR}/p_V were determined through other *NEOWISE* observations using *W*3 and/or *W*4 at a similar phase angle from Mainzer et al. (2011b). As described in Mainzer et al. (2011b, 2011d, 2011e) and Masiero et al. (2011), the differences in beaming between NEOs and Main Belt asteroids could represent real differences in thermal inertia and temperature distributions between these two populations. However, the phase angles at which NEOs and MBAs are observed by *NEOWISE* are generally quite different, meaning that more of the night side is observed for NEOs, which can also affect the beaming parameter. The correspondence between p_{IR}/p_V and taxonomic type for NEOs, MBAs, Hilda-group asteroids, and Jovian Trojans is described in Mainzer et al. (2011e), Mainzer et al. (2012b), Masiero et al. (2011), Grav et al. (2012a), and Grav et al. (2012b).

The distribution of bright versus dark NEOs appears similar to that observed at 12 μm during the fully cryogenic phase of the mission (Mainzer et al. 2011b). Through careful determination of the survey's biases with respect to albedo and orbital elements, it should be possible to extrapolate samples collected by *NEOWISE* to the larger population (cf. Mainzer et al. 2011b; Grav et al. 2011a, 2012a).

4.1. Comets

Infrared observations yield information regarding the nucleus, dust and gas of comets. Nucleus sizes for comets that are unobscured by dust or gas coma can be derived from the thermal component of the infrared flux. Comets must be closer than ~4 AU in order for the thermal signal from their nuclei to begin to dominate reflected sunlight at 4.6 μm (Bauer et al. 2013), if they are not active. However, by the time they reach ~3 AU, most comets are likely to become active (Wyckoff 1982). If active, reflected sunlight from the dust and molecular emission can dominate the signal at 4.6 μm. For active comets, infrared observations can constrain the distribution of dust, dust temperature, reflectance, production and particle size (cf. Bauer et al. 2011, 2012a, 2012b). Infrared observations sample dust that is larger than visible wavelengths and so set more definitive lower bounds on dust mass loss for comets (Bauer et al. 2008, 2012b).

NEOWISE bands also provide information on gas species produced by comets. A strong CO_2 ν_3-band emission line at 4.26 μm falls within the *W*2 bandpass, so *W*2 observations enable measurement of CO_2 production in comets. This line is obscured by Earth's atmosphere, but is detectable from space. Two effects must be mitigated to derive a CO_2 production rate. Dust signal must be estimated from the 3.4 μm band, but *W*1 provides only an upper bound on the dust signal. Additional visible wavelength brightness measurements from ground-based telescopes taken near the time of the *NEOWISE* observations serve to better constrain the dust production. A weaker CO line at 4.67 μm falls within the *W*2 bandpass (Bauer et al. 2011); therefore, estimating CO_2 production requires an

Table 2
Thermal Fit Results for the NEO Detections Reported in this Work

Name	Name	H	G	D (km)	p_V	η	p_{IR}	No. Obs. $W1$	No. Obs. $W2$
01627	1627	12.87	0.60	8.485 ± 0.292	0.174 ± 0.023	1.400 ± 0.500	0.253 ± 0.031	13	14
02102	2102	16.00	0.15	1.323 ± 0.134	0.383 ± 0.066	0.733 ± 0.076	0.614 ± 0.105	16	16
03554	3554	15.87	0.15	2.419 ± 0.600	0.142 ± 0.065	2.120 ± 0.428	0.283 ± 0.151	22	24
04954	4954	12.75	0.15	9.494 ± 0.244	0.156 ± 0.023	1.400 ± 0.500	0.302 ± 0.061	11	11
07025	7025	17.94	0.15	0.510 ± 0.171	0.452 ± 0.268	1.400 ± 0.555	0.724 ± 0.273	0	9
25916	25916	13.40	0.15	6.130 ± 0.159	0.205 ± 0.026	1.400 ± 0.500	0.234 ± 0.053	16	20
35107	35107	16.98	0.15	1.197 ± 0.402	0.199 ± 0.241	1.400 ± 0.475	0.319 ± 0.274	0	16
40267	40267	15.40	0.15	2.437 ± 0.326	0.199 ± 0.100	1.400 ± 0.179	0.323 ± 0.181	5	5
55532	55532	16.10	0.15	1.294 ± 0.950	0.383 ± 0.210	1.400 ± 0.863	0.448 ± 0.299	7	7
85182	85182	17.10	0.15	1.098 ± 0.342	0.212 ± 0.188	1.400 ± 0.423	0.339 ± 0.288	0	9
85628	85628	16.90	0.15	0.952 ± 0.188	0.339 ± 0.121	2.100 ± 0.451	1.000 ± 0.207	0	11
85774	85774	19.20	0.15	0.606 ± 0.072	0.100 ± 0.022	1.092 ± 0.116	0.160 ± 0.035	11	12
89355	89355	15.60	0.15	2.668 ± 0.957	0.139 ± 0.173	1.835 ± 0.587	0.223 ± 0.274	25	27
90075	90075	15.10	0.15	2.857 ± 0.879	0.197 ± 0.158	1.400 ± 0.373	0.316 ± 0.323	0	5
90367	90367	17.70	0.15	1.648 ± 0.671	0.054 ± 0.052	1.400 ± 0.442	0.087 ± 0.130	0	12
D8127	138127	17.00	0.15	0.460 ± 0.108	0.497 ± 0.282	1.400 ± 0.375	0.497 ± 0.250	7	7
E2781	142781	16.10	0.15	1.319 ± 0.353	0.374 ± 0.109	0.805 ± 0.227	0.596 ± 0.173	15	17
G2080	162080	19.80	0.15	0.479 ± 0.036	0.092 ± 0.014	0.927 ± 0.062	0.148 ± 0.022	6	6
G3691	163691	17.00	0.15	3.000 ± 1.053	0.031 ± 0.042	1.400 ± 0.377	0.050 ± 0.038	0	7
I6823	186823	19.10	0.15	0.842 ± 0.346	0.057 ± 0.030	1.400 ± 0.490	0.091 ± 0.220	0	5
O2450	242450	14.70	0.15	3.320 ± 1.032	0.322 ± 0.192	1.400 ± 0.457	0.516 ± 0.267	12	12
P0620	250620	18.10	0.15	0.864 ± 0.306	0.136 ± 0.065	1.400 ± 0.490	0.218 ± 0.286	0	7
Q2623	262623	18.50	0.15	0.444 ± 0.160	0.357 ± 0.263	1.400 ± 0.564	0.571 ± 0.287	0	6
Q9690	269690	18.50	0.15	0.879 ± 0.342	0.091 ± 0.055	1.400 ± 0.475	0.146 ± 0.221	0	9
R1480	271480	17.50	0.15	0.672 ± 0.220	0.392 ± 0.290	1.400 ± 0.507	0.627 ± 0.348	0	7
R6468	276468	17.90	0.15	1.312 ± 0.373	0.071 ± 0.052	1.400 ± 0.322	0.114 ± 0.139	0	5
U4330	304330	18.90	0.15	1.079 ± 0.151	0.037 ± 0.020	2.637 ± 0.300	0.059 ± 0.032	15	15
X4673	334673	17.80	0.15	0.674 ± 0.250	0.295 ± 0.190	1.400 ± 0.505	0.472 ± 0.262	0	13
b7732	377732	17.00	0.15	0.886 ± 0.261	0.352 ± 0.145	0.945 ± 0.297	0.566 ± 0.226	6	7
c1677	381677	18.40	0.15	0.740 ± 0.168	0.140 ± 0.186	2.520 ± 0.563	0.223 ± 0.296	15	19
c7733	387733	19.00	0.15	0.442 ± 0.137	0.284 ± 0.196	1.400 ± 0.491	0.987 ± 0.183	5	6
c9694	389694	18.20	0.15	0.734 ± 0.100	0.172 ± 0.061	0.544 ± 0.083	0.276 ± 0.098	5	7
J98S15B	1998 SB15	21.00	0.15	0.283 ± 0.105	0.088 ± 0.085	1.400 ± 0.477	0.141 ± 0.170	0	15
J99S10K	1999 SK10	19.70	0.15	0.259 ± 0.042	0.346 ± 0.105	0.597 ± 0.111	0.554 ± 0.168	7	7
K00AK5G	2000 AG205	19.70	0.15	0.598 ± 0.032	0.065 ± 0.011	0.691 ± 0.036	0.104 ± 0.018	15	19
K02X40S	2002 XS40	20.10	0.15	0.617 ± 0.044	0.042 ± 0.008	1.141 ± 0.074	0.068 ± 0.013	14	14
K03C11C	2003 CC11	19.10	0.15	1.221 ± 0.600	0.027 ± 0.024	1.400 ± 0.512	0.043 ± 0.060	0	17
K04M02X	2004 MX2	19.30	0.15	1.100 ± 0.135	0.028 ± 0.010	0.973 ± 0.107	0.045 ± 0.016	7	8
K07B00G	2007 BG	19.50	0.15	0.623 ± 0.107	0.072 ± 0.023	1.443 ± 0.226	0.115 ± 0.036	3	6
K08Q11S	2008 QS11	19.90	0.15	0.472 ± 0.195	0.087 ± 0.088	1.400 ± 0.499	0.139 ± 0.141	0	13
K09D01M	2009 DM1	17.00	0.15	1.242 ± 0.283	0.192 ± 0.049	1.042 ± 0.214	0.308 ± 0.079	49	53
K09U17X	2009 UX17	21.60	0.15	0.566 ± 0.186	0.013 ± 0.010	1.400 ± 0.416	0.020 ± 0.082	0	15
K10L14J	2010 LJ14	17.80	0.15	0.842 ± 0.255	0.189 ± 0.130	1.400 ± 0.407	0.302 ± 0.335	0	22
K10O01Q	2010 OQ1	19.00	0.15	0.722 ± 0.252	0.085 ± 0.070	1.400 ± 0.459	0.136 ± 0.254	0	11
K13P06X	2013 PX6	18.40	0.15	1.855 ± 0.162	0.022 ± 0.006	1.265 ± 0.095	0.036 ± 0.010	9	10
K13W44T	2013 WT44	19.30	0.15	1.319 ± 0.109	0.019 ± 0.004	1.496 ± 0.103	0.031 ± 0.006	5	6
K13Y13Z	2013 YZ13	19.60	0.15	0.475 ± 0.202	0.113 ± 0.141	1.400 ± 0.529	0.181 ± 0.213	0	6
K13YD9P	2013 YP139	20.60	0.15	0.968 ± 0.316	0.011 ± 0.010	1.400 ± 0.393	0.017 ± 0.020	6	6
K14A33A	2014 AA33	19.30	0.15	1.271 ± 0.209	0.021 ± 0.005	2.108 ± 0.273	0.033 ± 0.008	5	5
K14A46Q	2014 AQ46	20.30	0.15	0.839 ± 0.359	0.019 ± 0.010	1.400 ± 0.495	0.030 ± 0.069	0	11
K14A53A	2014 AA53	19.80	0.15	0.710 ± 0.338	0.042 ± 0.025	1.400 ± 0.566	0.067 ± 0.219	0	14
K14B60G	2014 BG60	20.10	0.15	0.746 ± 0.206	0.029 ± 0.020	1.400 ± 0.346	0.046 ± 0.145	0	187
K14B63E	2014 BE63	21.20	0.15	0.599 ± 0.238	0.016 ± 0.015	1.400 ± 0.469	0.026 ± 0.053	0	6
K14C04Y	2014 CY4	21.50	0.15	0.450 ± 0.204	0.022 ± 0.020	1.400 ± 0.547	0.035 ± 0.074	0	7
K14C14F	2014 CF14	17.90	0.15	0.864 ± 0.246	0.164 ± 0.085	1.400 ± 0.398	0.262 ± 0.306	0	6
K14D10C	2014 DC10	20.10	0.15	0.637 ± 0.028	0.040 ± 0.010	0.991 ± 0.041	0.063 ± 0.016	8	10
K14E00D	2014 ED	19.20	0.15	0.381 ± 0.098	0.254 ± 0.137	1.400 ± 0.372	0.407 ± 0.266	0	6
K14E45N	2014 EN45	20.85	0.15	0.814 ± 0.311	0.012 ± 0.010	1.400 ± 0.460	0.019 ± 0.044	0	14
K14E49Q	2014 EQ49	21.20	0.15	0.356 ± 0.117	0.046 ± 0.045	1.400 ± 0.392	0.074 ± 0.079	0	6

Notes. This table contains the preliminary thermal fit results based on the first-pass version of the *NEOWISE* data processing as described in the text. The columns contain object name, H magnitude, phase curve slope parameter G, diameter, visible albedo p_V, beaming parameter η, infrared albedo p_{IR}, and number of observations in each of the two *NEOWISE* bands. The $1-\sigma$ errors presented here were statistically generated using Monte Carlo modeling. *NEOWISE* magnitudes, absolute magnitude H, and G were varied by their $1-\sigma$ error bars, as well as beaming (η) and p_{IR} when these two parameters could not be fit. The statistical errors on diameter and p_V for each object in the table should be added in quadrature to the systematic errors described in the text and discussed in Mainzer et al. (2012b).

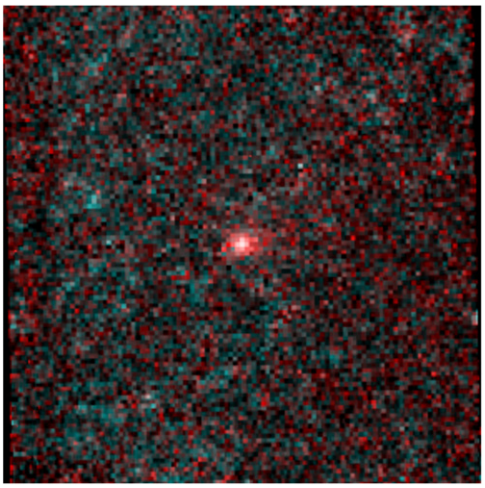

Figure 16. Comoving coadd of Comet C/2014 C3 *NEOWISE*; color-coding is identical to that in Figure 3.

(A color version of this figure is available in the online journal.)

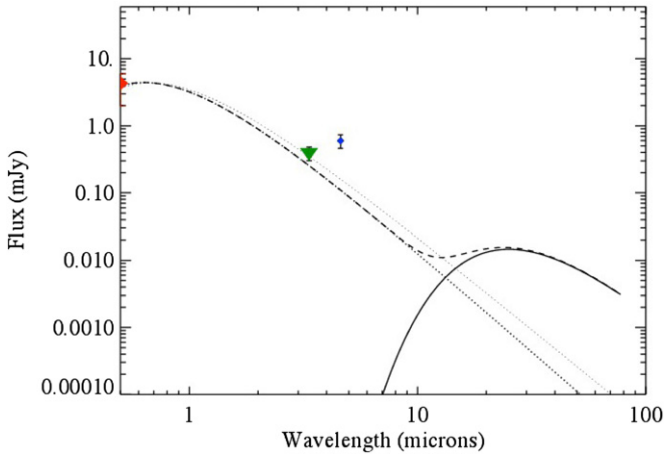

Figure 17. Model for the dust in C/2013 A1 Siding Spring is shown; excess *W*2 emission above the dust signature indicates the presence of CO_2 or CO. The dust signal scales as the reflected light flux and thermal flux combined based on $Af\rho$ values in *W*1 and the visual wavelength measurement (red diamond on the left hand side) reported in Williams (2014). The thermal flux is modeled assuming a blackbody temperature T_{bb} of 146 K appropriate for the comet's heliocentric distance of 3.82 AU at the time of observation. *W*1 and *W*2 fluxes are indicated by the green triangle and blue diamond, respectively. The spectrum of reflected light, assuming a neutral spectral response and a particle size distribution (PSD) that scales as the particle size to the −3 power is the heavy dotted line. The same with reddening law from Jewitt & Meech (1986) is shown by the dotted line. A PSD with a −3 power law accounts for the stronger signal at visual wavelengths shown in the plot, since smaller particles do not emit efficiently at longer wavelengths. The solid line is the thermal flux for $T_{bb} = 146$ K for the same projected dust area as indicated by the $Af\rho$ value (log-cm of 2.5). The combined flux for the neutrally reflecting dust is shown by the heavy dashed line. For each case of dust behavior scaled to the *W*1 signal, the *W*2 signal is still greater than can be accounted for by the model dust component. This result yields a *W*2 excess of ∼ 0.3–0.5 mJy for an 11 arcsec aperture, and a derived CO_2 production of $2.7 \pm 0.5 \times 10^{26}$ mol s^{-1}, assuming all the *W*2 excess was due to CO_2, and $2.9 \pm 0.5 \times 10^{27}$ mol s^{-1} if the excess was caused by CO alone.

(A color version of this figure is available in the online journal.)

assumption that the signal is not dominated by CO. Such an assumption is not unreasonable, since per molecule, the CO signal is on the order of 11 times weaker. However, it is not possible to distinguish between the two molecules without further supposition of what the comet's composition is likely to be. Thus excess *W*2 signal formally provides a lower bound on the CO_2 and CO production, while providing an upper bound on one species or another.

To date, 10 comets have been detected during the reactivated *NEOWISE* mission. Half of these objects are long-period comets, with orbital periods greater than 200 yr. Among them is the comet C/2013 A1 Siding Spring, which is due to pass within 150,000 km of the surface of Mars on 2014 October 19. Comet C/2014 C3 *NEOWISE*, a retrograde Halley family comet with a period of 110 yr, is the first cometary body discovered during the reactivated *NEOWISE* mission (Figure 16). At present, cometary activity is initially detected in the *NEOWISE* data by visual inspection, but automatic detection routines are being evaluated.

A preliminary analysis of *NEOWISE* images of C/2013 A1 Siding Spring was conducted on the data obtained from the first month of observation. *NEOWISE* observed comet Siding Spring in seven exposures in *W*1 and *W*2 on 2014 January 16. The S/N measured on each frame exceeded 10 in each band. The *W*1 and *W*2 fluxes were 0.4 ± 0.1 and 0.60 ± 0.14 mJy, respectively (Figure 17).

$Af\rho$, a measure of dust production in comets, is the product of the dust grain albedo, A, the filling factor, f, of grains that fall within a circular photometry aperture, and the linear radius, ρ, of the aperture at the comet's distance. $Af\rho$ can be determined from the measured comet fluxes and the comet's known distance (A'Hearn et al. 1984). We found $Af\rho$ values of 2.4–2.5 log-cm. Assuming grain reflectance values of ∼0.04, similar to those found for other cometary dust grains (cf. Bauer et al. 2012a), and grain densities near those of water-ice, the corresponding dust production values were ∼100 kg s^{-1} for ejection velocities on the order of 250 m s^{-1}. Assuming a common particle size frequency distribution with log-slope ∼ −3 with grain radius (Fulle 2004), the dust signal within *W*2 represents only 30%–50% of the total signal. The derived *W*2 flux excess can be attributed to CO_2 production on the order of 10^{26} molecules per second, or a CO production rate of $\sim 10^{27}$ molecules per second.

5. CONCLUSIONS

The reactivated *NEOWISE* mission is conducting a survey with multiple coverages of the entire sky at 3.4 and 4.6 μm over three years. Data quality has remained essentially unchanged from the prime mission's post-cryogenic phase, despite 32 months of hibernation. The data will allow for the characterization and discovery of minor planets and will enable a wide range of time-domain studies. The mission will result in measurements of radiometric diameters and albedos for ∼20% of the known NEO population over the course of three years.

This publication makes use of data products from *NEOWISE*, which is a project of the Jet Propulsion Laboratory/California Institute of Technology, funded by the National Aeronautics and Space Administration. This publication makes use of data products from the *Wide-field Infrared Survey Explorer*, which is a joint project of the University of California, Los Angeles, and the Jet Propulsion Laboratory/California Institute of Technology, funded by the National Aeronautics and Space Administration. We thank the paper's referee for helpful comments that greatly improved the manuscript. We gratefully acknowledge the services specific to *NEOWISE* contributed by the International Astronomical Union's Minor Planet Center, operated by the Harvard-Smithsonian Center for Astrophysics, and the Central Bureau for Astronomical Telegrams, operated by Harvard University. We also thank the worldwide community of dedicated amateur and professional astronomers devoted to

minor planet follow-up observations. This research has made use of the NASA/IPAC Infrared Science Archive, which is operated by the California Institute of Technology, under contract with the National Aeronautics and Space Administration.

REFERENCES

A'Hearn, M. F., Schleicher, D. G., Millis, R. L., Feldman, P. D., & Thompson, D. T. 1984, AJ, 89, 579
Bauer, J. M., Choi, Y.-J., Weissman, P. R., et al. 2008, PASP, 120, 393
Bauer, J. M., Grav, T., Blauvelt, E., et al. 2013, ApJ, 773, 22
Bauer, J. M., Kramer, E., Mainzer, A. K., et al. 2012a, ApJ, 758, 18
Bauer, J. M., Mainzer, A. K., Grav, T., et al. 2012b, ApJ, 747, 49
Bauer, J. M., Walker, R. G., Mainzer, A. K., et al. 2011, ApJ, 738, 171
Beichman, C. A., Neugebauer, G., Habing, H. J., et al. 1988, Infrared Astronomical Satellite (IRAS) Catalogs and Atlases. Volume 1: Explanatory Supplement, Vol. 1
Beletic, J. W., Blank, R., Gulbransen, D., et al. 2008, Proc. SPIE, 7021
Benner, L. A. M., Ostro, S. J., Magri, C., et al. 2008, Icar, 198, 294
Binzel, R. P., & Xu, S. 1993, Sci, 260, 186
Bowell, E., Hapke, B., Domingue, D., et al. 1989, in Asteroids II, ed. R. P. Binzel, T. Gehrels, & M. S. Matthews, 524
Buratti, B. J., Dalba, P. A., Hicks, M. D., et al. 2013, JGRE, 118, 1991
Carry, B. 2012, P&SS, 73, 98
Christou, A. A., & Asher, D. J. 2011, MNRAS, 414, 2965
Connors, M., Wiegert, P., & Veillet, C. 2011, Natur, 475, 481
Consolmagno, G. J., & Britt, D. T. 1998, M&PS, 33, 1231
Cutri, R. M., Wright, E. L., Conrow, T., et al. 2012, http://wise2.ipac.caltech.edu/docs/release/allsky/expsup/
Cutri, R. M., Wright, E. L., Conrow, T., et al. 2013, Explanatory Supplement to the AllWISE Data Release Products, Tech. Rep.
Cutri, R. M. e. 2014, yCat, 2328, 0
DeMeo, F. E., Binzel, R. P., Slivan, S. M., & Bus, S. J. 2009, Icar, 202, 160
DeMeo, F. E., & Carry, B. 2014, Natur, 505, 629
Durech, J., Sidorin, V., & Kaasalainen, M. 2010, A&A, 513, A46
Eddington, A. S. 1913, MNRAS, 73, 359
Fowler, J. W., & Chillemi, J. R. 1992, The IRAS Minor Planet Survey, Phillips Laboratory, Hanscom AF Base, MA, Tech. Rep., PL-TR-92-2049, 17
Fulle, M. 2004, in Motion of Cometary Dust, ed. M. C. Festou, H. U. Keller, & H. A. Weaver, 565
Grav, T., Jedicke, R., Denneau, L., et al. 2011a, PASP, 123, 423
Grav, T., Mainzer, A. K., Bauer, J., et al. 2011b, ApJ, 742, 40
Grav, T., Mainzer, A. K., Bauer, J., et al. 2012a, ApJ, 744, 197
Grav, T., Mainzer, A. K., Bauer, J. M., Masiero, J. R., & Nugent, C. R. 2012b, ApJ, 759, 49
Harris, A. W. 1998, Icar, 131, 291
Heinrichsen, I., & Wright, E. L. 2006, Proc. SPIE, 6270
Jewitt, D., & Meech, K. J. 1986, ApJ, 310, 937
Kubica, J., Denneau, L., Grav, T., et al. 2007, Icar, 189, 151
Larson, S. 2007, in IAU Symp. 236, Near Earth Objects, Our Celestial Neighbors: Opportunity and Risk, ed. G. B. Valsecchi, D. Vokrouhlický, & A. Milani (Cambridge: Cambridge Univ. Press), 323
Lebofsky, L. A., & Spencer, J. R. 1989, in Asteroids II, ed. R. P. Binzel, T. Gehrels, & M. S. Matthews (Tucson, AZ: Univ. Arizona Press), 128
Lebofsky, L. A., Sykes, M. V., Tedesco, E. F., et al. 1986, Icar, 68, 239
Mainzer, A., Bauer, J., Grav, T., et al. 2011a, ApJ, 731, 53
Mainzer, A., Bauer, J., Grav, T., et al. 2014, ApJ, 784, 110
Mainzer, A., Grav, T., Bauer, J., et al. 2011b, ApJ, 743, 156
Mainzer, A., Grav, T., Masiero, J., et al. 2012a, ApJL, 760, L12
Mainzer, A., Grav, T., Masiero, J., et al. 2011c, ApJ, 736, 100
Mainzer, A., Grav, T., Masiero, J., et al. 2011d, ApJL, 737, L9
Mainzer, A., Grav, T., Masiero, J., et al. 2011e, ApJ, 741, 90
Mainzer, A., Masiero, J., Grav, T., et al. 2012b, ApJ, 745, 7
Masci, F. 2013, in Astrophysics Source Code Library, ICORE: Image Coaddition with Optional Resolution Enhancement
Masci, F. J., & Fowler, J. W. 2009, in ASP Conf. Ser. 411, Astronomical Data Analysis Software and Systems XVIII, ed. D. A. Bohlender, D. Durand, & P. Dowler (San Francisco, CA: ASP), 67
Masiero, J. R., Mainzer, A. K., Grav, T., et al. 2011, ApJ, 741, 68
Masiero, J. R., Mainzer, A. K., Grav, T., et al. 2012, ApJL, 759, L8
Merline, W. J., Weidenschilling, S. J., Durda, D. D., et al. 2002, in Asteroids III, ed. W. F. Bottke, Jr., et al. (Tucson, AZ: Univ. Arizona Press), 289
Pravec, P., Harris, A. W., Kušnirák, P., Galád, A., & Hornoch, K. 2012, Icar, 221, 365
Reddy, V. 2010, PDSS, 127
Stevenson, R., Kramer, E. A., Bauer, J. M., Masiero, J. R., & Mainzer, A. K. 2012, ApJ, 759, 142
Stuart, J. S., & Binzel, R. P. 2004, Icar, 170, 295
Tabachnik, S. A., & Evans, N. W. 2000, MNRAS, 319, 63
Tedesco, E. F., Noah, P. V., Noah, M., & Price, S. D. 2002, AJ, 123, 1056
Tholen, D., & Barucci, M. 1989, in Asteroids II, ed. R. P. Binzel, T. Gehrels, & M. S. Matthews (Tucson, AZ: Univ. Arizona Press), 298
Thomas, C. A., Trilling, D. E., Emery, J. P., et al. 2011, AJ, 142, 85
Warner, B. D., Harris, A. W., & Pravec, P. 2009, Icar, 202, 134
Williams, G. V. 2014, MPEC, 43
Wright, E. L., Eisenhardt, P. R. M., Mainzer, A. K., et al. 2010, AJ, 140, 1868
Wyckoff, S. 1982, in IAU Colloq. 61: Comet Discoveries, Statistics, and Observational Selection, ed. L. L. Wilkening (Washington, DC: AAS), 3
Xu, S., Binzel, R. P., Burbine, T. H., & Bus, S. J. 1995, Icar, 115, 1